Broadband Acoustic Wave Suppression via Total Internal Reflection in Phase Gradient Curved Metasurfaces

Shuzhen Huang[1], Lei Zhang[2*], Guilin Wen[3], Zi Wen Tham[2], Shan Yin[1], Jie Liu[3]

[1]State Key Laboratory of Advanced Design and Manufacture for Vehicle Body, Hunan University, Changsha, Hunan 410082, China.

[2]Institute of Materials Research and Engineering (IMRE), Agency for Science, Technology and Research (A*STAR), 2 Fusionopolis Way, Innovis #08-03, Singapore 138634, Republic of Singapore.

[3]School of Mechanical Engineering, Yanshan University, Qinhuangdao, Hebei 066004, China.

Abstract:

Vibration suppression remains a persistent challenge in engineering applications. Elastic metasurfaces have emerged as a promising solution, yet many existing designs rely on slotting and narrow-band structures, which compromise structural integrity and limit practical uses. In this work, a surface mounted phased gradient curved metasurface (PGCM) is designed based on the generalized Snell's law and the theory of total internal reflection for broadband Lamb waves suppression. By adjusting the height of the curved beam, the phase of transmitted Lamb waves can be modulated over a 2π range. The dimensions of the cell structure are optimized through theoretical analysis and numerical simulation. The broadband wave suppression capabilities of the PGCM are thoroughly investigated and experimentally validated. Compared to existing metasurface designs, the PGCM effectively suppresses both normal incident Lamb waves and omnidirectional incident waves. Simulations show a maximum wave suppression of 39.72 dB for normal incidence and 21.34 dB for omnidirectional incidence, with a robust bandwidth effect under both conditions. Experimental results verify the wave suppression performance and bandwidth effect. The structure is simple, cost-effective, and suitable for surface mounting. This work provides an innovative solution for acoustic wave suppression.

Key Words: Elastic metasurface, phase gradient, total internal reflection; acoustic waves, vibration control

* Corresponding author, email: zhangl@imre.a-star.edu.sg

1. Introduction

Vibration suppression is important for maintaining the stability and reliability of high-precision equipment [1]. Traditional vibration control systems often rely on specialized damping devices [2-7] and additional equipment, which significantly increase the overall size and mass of the structure, compromising system performance. Artificial periodic structures, such as metamaterials [7-10] and phononic crystals [11-14], typically achieve vibration control through local resonance absorption. However, their relatively large size limits their application in industries like aerospace and automotive manufacturing.

The introduction of acoustic metasurfaces [16] has revolutionized the field. The acoustic metasurfaces have attracted widespread attention for their lightweight design, flexibility, and precise directional control [17-25]. The acoustic metasurfaces have enabled remarkable acoustic phenomena such as acoustic focusing [20,21], absorption [22,23], and asymmetric transmission [24,25]. Similarly, elastic metasurfaces hold significant research value in the study of elastic waves. For vibration control, elastic metasurfaces offer more efficient and flexible solutions [26-29]. It surpasses traditional vibration suppression methods by overcoming wavelength-scale limitations. For example, Zhu et al. [30-32] introduced total internal reflection metasurfaces, demonstrating that they act as hard barriers to acoustic waves at specific frequencies, achieving significant vibration isolation. However, these designs often involve embedding complex internal structures in substrates, compromising structural stiffness and limiting their use in load-bearing applications. Similarly, Cao et al. [27] proposed a metasurface for vibration reduction and sound absorption that required grooves in the host structure, creating beam-like elements of varying lengths. Such methods typically involve modifications like holes, grooves [33-44] or nested in the substrate [35,40-41] to achieve phase modulation, which damages structural integrity, increases manufacturing complexity, and limits practical applications. To maintain structural integrity, Yang et al. [45] developed a curved beam metasurface to regulate Lamb waves. However, this design lacked experimental validation. Other researchers have manipulated flexural waves by adding vertical pillars to plates [29,46-51]. For instance, Cao et al. [29,50,51] introduced elastic metasurfaces with cylindrical resonators to control flexural waves through interference. Yet, the large number of resonators increased complexity, and their broadband effects remained unexplored. Overall, the existing studies on elastic metasurfaces for vibration suppression often fail to balance the structural integrity with vibration suppression performance.

In view of the existing limitations, this study demonstrates a surface mounted phased gradient curved metasurface (PGCM) structure based on periodic curved beam structures which can delay the phase of transmitted Lamb waves. By leveraging this principle, we design a curved beam metasurface that suppresses acoustic waves from omnidirectional incident waves based on the theory of total internal reflection (TIR). By modulating the full 2π phase range of transmitted Lamb waves through adjustable beam heights, this design improves the adaptability to practical environmental conditions compared to the conventional curved beam periodic structures. Without compromising the host structure, the gaps in adjacent cells minimize the coupling effects, enhancing the acoustic suppression performance. The proposed metasurface offers a promising solution for practical engineering applications, with potential use in fields such as aerospace, machinery manufacturing, and the automotive industry. For instance, in the machinery manufacturing sector, computerized numerical control (CNC) machines require effective vibration isolation to ensure high machining accuracy and safe, stable operation.

In this paper, we investigate the broadband vibration suppression performance of the proposed acoustic metasurface structure through numerical simulation and validate its performance experimentally. The remainder of this paper is organized as follows: Section 2 introduces the theory and the design of the metasurface and its vibration suppression performance. Section 3 presents experimental validation of the PGCM's vibration suppression effectiveness and the reliability of the proposed model. Finally, Section 4 concludes the paper.

2. Design and Simulation

2.1 Theory

Zhu et al. [30–32] demonstrated that metasurfaces can achieve critical angle conditions like the phenomenon of total internal reflection. This occurs when a wave travels between two media with differing refractive indices, and the incident angle exceeds the critical angle, resulting in the complete reflection of the incident wave without any refraction. Similarly, a metasurface can be designed to control incident waves w_i so that they can be mostly reflected without substantial refraction as shown in Fig.1.

The Generalized Snell's law is shown in Eq. (1),

$$n_t \sin\theta_t - n_i \sin\theta_i = \frac{\lambda_p \mathrm{d}\varphi}{2\pi \mathrm{d}y} \tag{1}$$

where n_t, n_i are the refractive indices of the refracting medium and the incident medium respectively. When the thin plate materials of the incident space and the refraction space are both aluminum alloy, $n_t = n_i = n = 1.2$. θ_t, θ_i are the refraction angle and the incident angle, respectively, λ_p is the wavelength of the Lamb waves in the plate at the corresponding frequency f, φ is the phase of the transmitted waves, $\mathrm{d}\varphi/\mathrm{d}y$ is the phase gradient along the y direction.

When the above equation has no real solution, the total internal reflection occurs. As $-1 < \sin\theta_t < 1$, $-1 < \sin\theta_i < 1$, the equation has no real solutions when $\lambda_p \mathrm{d}\varphi/(2\pi n \mathrm{d}y) \geqslant 2$. Thus, the critical angle condition for the metasurface to achieve total internal reflection is $\lambda_p \mathrm{d}\varphi/(2\pi n \mathrm{d}y) = 2$.

The phase gradient at the critical angle condition is therefore $\mathrm{d}\varphi/\mathrm{d}y = 4\pi n/\lambda_p$. Under this critical angle condition, the phase at different positions along y is a linear function of the y value. Thus, the total width of the unit L in the 2π period is $L = 4\pi \mathrm{d}y/\mathrm{d}\varphi = \lambda_p/(2n)$.

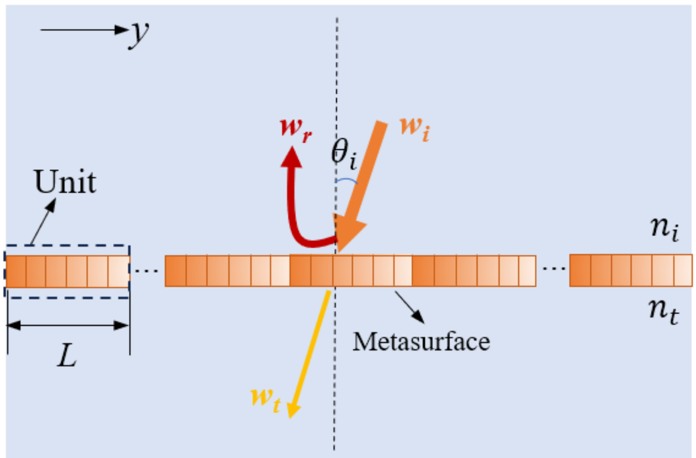

Fig.1. Illustrative metasurface design based on total internal reflection.

2.2 Cell structure

The proposed cell structure of the curved beam metasurface is shown in Fig.2(b). The curved structure is designed according to the equation $z_i(x) = h_i(1\text{-}\cos\pi x/1.7\text{a})$, where $x \in$ (0,3.4a), a is a constant, i is the cell number, and h_i is the half height of the cell structure i.

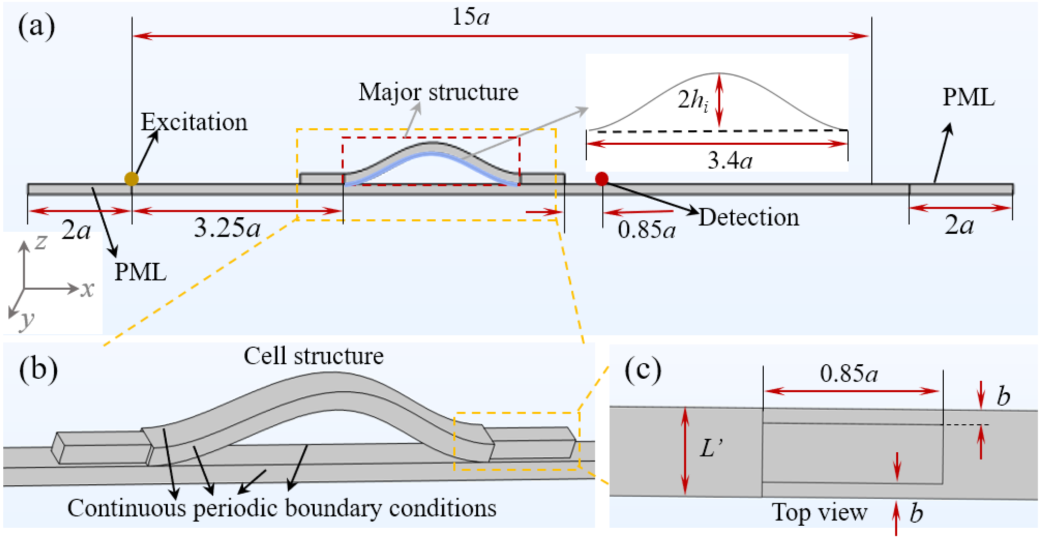

Fig.2. Numerical simulation model diagram for quantitative evaluation of flexural waves passing through functional cell (a). The locally enlarged subgraphs (b) and (c). Cell structure (b) and top view of the support structure.

Fig.2(a) shows the finite element model for a cell structure. The structural mechanics physics is selected in the multi-physics simulation software COMSOL for simulation. The material properties of the thin plate and designed metasurface structure are shown in Table 1. Both sides of the thin plate and the major structure of the cell are set as continuous periodic boundary conditions. The displacement amplitude of the excitation is 1mm. Perfectly matched layers (PML) are set at the left and right ends to maximize the absorption of reflected energy from the thin plate. The structural dimensions are indicated in Fig.2, where a is selected as 10 mm in the simulation. To reduce the coupling effect between adjacent curved beam structures in a metasurface structure, the direct contact between adjacent cell structures should be reduced as much as possible, so a gap b is set between the support structures at the two ends of the adjacent cell structures (Fig.2(c)). Considering the manufacturing accuracy, b is assigned to be 1 mm.

Table 1 Material properties of the curved metasurface and plate

Parameters	Young modulus E (GPa)	Density ρ (kg/m^3)	Poisson's ratio σ
Values	72.4	2770	0.33

At low frequencies, the out-of-plane displacement amplitude of the antisymmetric mode A_0 is typically larger than that of other modes. Therefore, in this paper, only the A_0 mode is studied. Based on the Rayleigh-Lamb equation and the equation of flexural waves, the wavelength in the thin plate with a thickness of d = 2.00 mm, $\lambda_p = 23.46$ mm, when the excitation frequency f =15 kHz.

According to the wave equation [52], the sound waves propagate through the curved beam $z_c(t)$ and the plate $z_p(t)$ and respectively satisfies the following equations at the interference time t:

$$z_c(t) = \mathrm{A}\sin(k_c s\text{-}\omega t+\varphi_c) \tag{2}$$

$$z_p(t) = \mathrm{B}\sin(k_p s\text{-}\omega t+\varphi_p) \tag{3}$$

The phase change of a cell is related to its curvature by $\varphi_c = k_c s$, where $k_c = 2\pi/\lambda_c$ is the wave number in the beam at frequency f, $\lambda_c = \pi^2 E d_c^{\ 2}/(3\rho f^2)$ [53-55] is the wavelength of the beam at the frequency f. $\omega = 2\pi f$ is the angular frequency. $d_c = 2$ mm is the thickness of the curved beam, E is the Young's modulus and the ρ is the density of the curved structure. s is the wave path of the curve under the major structure. $\varphi_p = k_p$ is the phase difference that the thin plate corresponds to the span of the curved beam. A and B are the amplitudes of the Lamb wave propagation through the curved beam and the thin plate respectively. The corresponding interference wave $z(t)$ satisfies the following equation.

$$z(t) = z_c(t)+z_p(t) = [\mathrm{A}\cos(k_c s+\varphi_c)+\mathrm{B}\cos(k_p s+\varphi_p)]\sin(-\omega t)$$
$$+[\mathrm{A}\sin(k_c s+\varphi_c)+\mathrm{B}\sin(k_p s+\varphi_p)]\cos(-\omega t) \tag{4}$$

Let $m = [\mathrm{A}\cos(k_c s+\varphi_c)+\mathrm{B}\cos(k_p s+\varphi_p)]$, $q = [\mathrm{A}\sin(k_c s+\varphi_c)+\mathrm{B}\sin(k_p s+\varphi_p)]$, that is

$$z(t)=\sqrt{m^2+q^2}\sin(-\omega t+\varphi_0) \tag{5}$$

$$\tan\varphi_0=\frac{q}{m}=\frac{sin(k_c s+\varphi_c)+(\mathrm{B/A})sin(k_p s+\varphi_p)}{\cos(k_c s+\varphi_c)+(\mathrm{B/A})\cos(k_p s+\varphi_p)} \tag{6}$$

where B/A=0.1, φ_{ci} is the phase difference through the curved beam and i corresponds to 19 units selected randomly in the range of 2π. Then, connect the above relationship to get the value of the corresponding s_i. s_i can also be obtained by curve integration as shown below.

$$s_i=\int_0^{3.4\mathrm{a}}\sqrt{1+(z_i'(x))^2}\,\mathrm{d}x \tag{7}$$

where $z_i'(x)$ is the first derivative of $z_i(x)$. Then the functional relationship about h is solved by numerical analysis software, and the h_i corresponding to φ_{ci} is obtained as shown in Eq. (8).

$$\varphi_{ci}=k_c\int_0^{3.4\mathrm{a}}\sqrt{1+\left(\frac{\pi h_i}{1.7\mathrm{a}}\right)^2\left[\sin\left(\frac{\pi x}{1.7\mathrm{a}}\right)\right]^2}\,\mathrm{d}x \tag{8}$$

h_i is brought into the simulation model as shown in Fig. 2, and the simulation results of the cells corresponding to h_i were obtained. Figure 3 shows the comparison between the theoretical and simulated phases for 19 cells with phases ranging from – π to π. The red dots represent the theoretical initial setting values, while the black squares correspond to the numerical simulation results. The two results exhibit a strong agreement in overall trend, though some discrepancies are present. These deviations can be attributed to two factors: (1) the influence of reflected waves and (2) the contact between adjacent structures despite the grooved cell design, leading to incomplete elimination of coupling effects

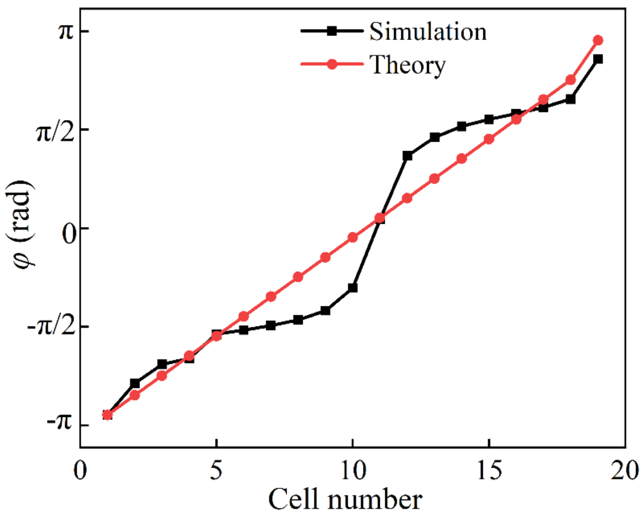

Fig.3. Comparison between theoretical analysis model and numerical simulation results.

The above results show that if more precise regulation is to be achieved, numerical simulation models should be given priority for quantitative design. Fig. 4 shows the numerical simulation results of the cell structure with different h. The results show that when different h values are selected, the phase picked up at the detection position covers a range of 2π.

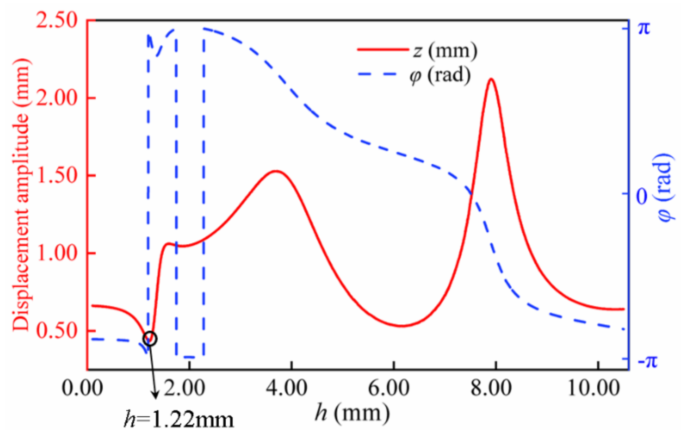

Fig.4. The z-direction out-of-plane displacement and phase distribution corresponding to the cell structure with different h.

The phase accumulation arises from the variation in wave propagation paths within the curved beam structures. Specifically, as the height of the curved beam increases, the effective propagation distance for Lamb waves also increases. This leads to a corresponding change in the transmitted wave phase, as governed by the wave equations provided in Eqs. (2) and (3). The transmitted Lamb waves from the metasurface and the base plate interfere at the structural junction. Changes in the propagation distance modify the phase of the transmitted waves, which in turn affects the phase of the resulting interference pattern. This controllable phase modulation forms the foundation of the phase gradient design. Fig.5 shows the simulation results for 6 cell structures designed for different phases. Fig. 5(a) shows that a phase distribution with a gradient of 0.4π, i.e., −π, −0.6π, −0.2π, 0.2π, 0.6π, and π, respectively, is realized. The width of the cell structure is $L' = L/6$. The corresponding h values for the 6 cells are 1.75 mm, 8.37 mm, 7.81 mm, 6.53 mm, 4.08 mm, and 2.28 mm, respectively. It is observed that the maximum height (2h) of the cell structure is 16.74 mm, while the wavelength is 23.46 mm. Therefore, in the vertical direction, the structure's thickness is less than the wavelength, indicating that it operates at a subwavelength scale. The out-of-plane (z-direction) displacement field distributions are shown in Fig. 5(b).

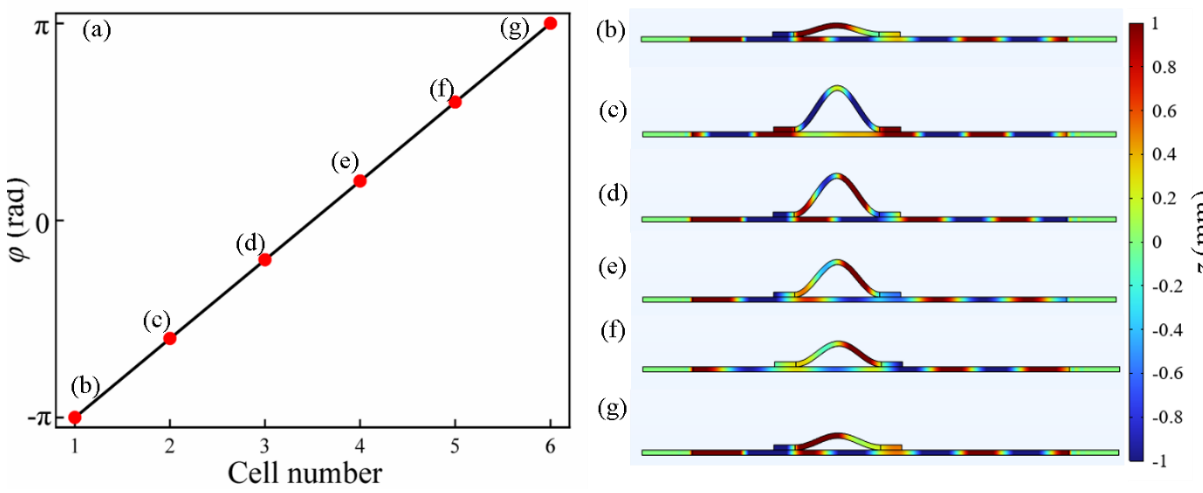

Fig.5. (a) Phase distribution of 6 cell structures in one periodic unit. (b) Out-of-plane displacement field distribution of the functional cell at the corresponding phase position.

2.3 Metasurface design and simulation

By assembling the 6 cell structures as shown in Fig. 5(b), a periodic unit of phase gradient curved metasuface (PGCM) can be formed. Fig.6(c) shows the acoustic metasurface made of 8 periods of the PGCM units, with total of 48 cells. Finite element simulations were conducted to evaluate the acoustic wave suppression performance of the PGCM in comparison with bare plate structure Fig.6(a) and a non-phase-gradient curved metasuface (n-PGCM) (Fig.6(b)). The n-PGCM comprises of curved metasurface cells of constant height. According to Fig.4, when h=h_0=1.22 mm, the out-of-plane displacement of the transmitted waves of the cell structure is the lowest. This unit is arrayed periodically to form the n-PGCM as shown in Fig.6(b), which is used to compare with the PGCM. The purpose of this comparison is to show whether the PGCM design has any effect in addition to the effect of the curved beam structure itself. PMLs are set on the left and right sides of the thin plate, and continuous periodic boundary conditions are set on the upper and lower boundaries. Continuous periodic boundary conditions are set on both sides of the main structure of PGCM at the edge.

Rectangular areas of 101 mm (L) × 111 mm (W) are selected for each plate, denoted as S0, S1 and S2 as shown in Figs.6(a)-(c). The left edges of S1 and S2 are 7.5 mm away from the metasurfaces. The average out-of-plane displacement of the area is calculated for comparison.

Fig. 6(d) illustrates the displacement field distribution of the bare plate under Excitation 1, a line excitation source represented by the green line in Fig. 6(a). Fig. 6(e) presents the displacement field distribution of the plate with n-PGCM, while Fig.6(f) depicts the displacement field distribution of the plate with PGCM. The color bars indicating the displacement fields are adjusted to the same scale for consistency.

It is evident that the displacement field transmitted through the n-PGCM is attenuated compared to that of the bare plate, which shows the vibration suppression capability of this metasurface structure. This observation also partially validates the numerical simulation accuracy of the cell structure. In contrast, Fig. 6(g) shows that the displacement amplitude of the plate with the PGCM is significantly smaller compared to Fig.6(e) and Fig.6(f), signifying that the PGCM structure, based on the total internal reflection design, achieves superior vibration suppression than the n-PGCM. Nonetheless, a small portion of the vibration is still diffracted through the gaps between the metasurface cells into the transmission space.

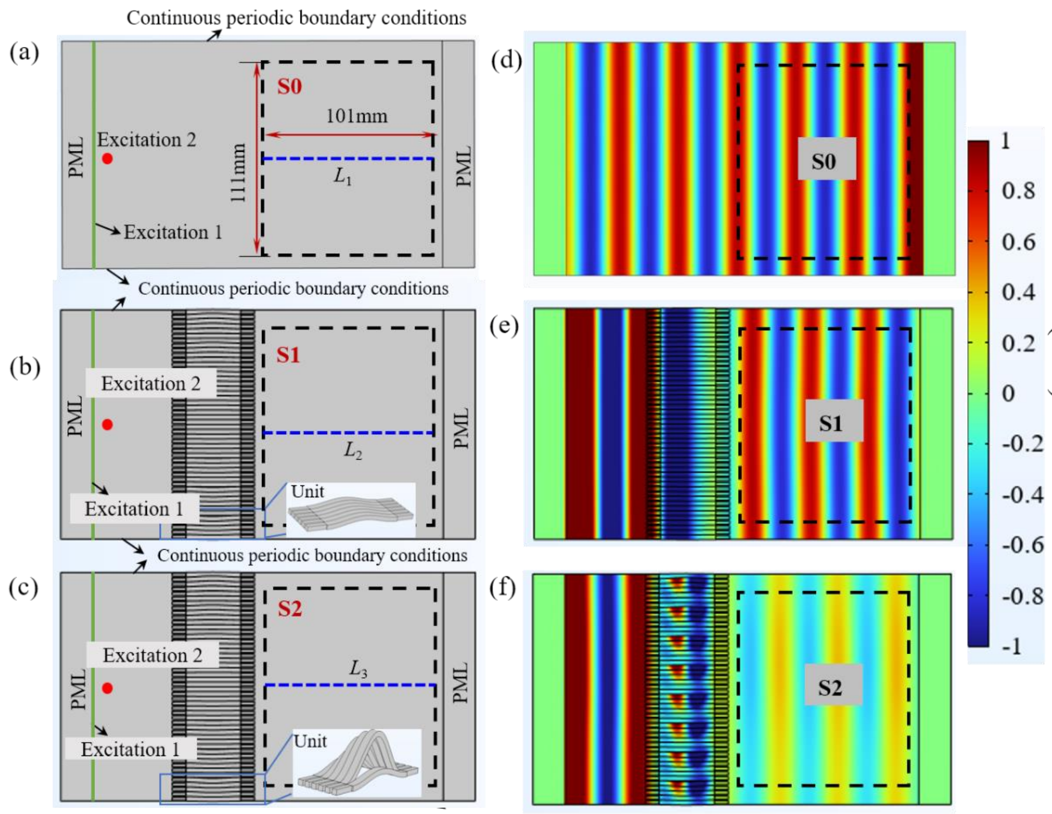

Fig.6. The simulation model and schematic diagram of (a) the bare plate, (b) the plate with n-PGCM, and (c) the plate with PGCM. (d)-(f) are the displacement field distributions corresponding to bare plate, plate with n-PGCM, and PGCM, respectively.

To quantitatively evaluate the acoustic suppression performance of the elastic metasurfaces, the wave suppression level, *Sup_lev*, as defined in Eq. (9), is introduced to evaluate the Lamb wave suppression effect of the curved metasurfaces.

$$Sup\_lev = 20\log(A_p/A_t) \tag{9}$$

where A_p and A_t are the displacement amplitudes of the Lamb waves in the bare plate structure and plate structure with metasurfaces. When the value is more than 0 dB, the wave suppression effect is effective, and a larger value indicates that the wave suppression effect is better. When $A_p/A_t = 2$, the wave suppression level is 6 dB, which means it has an excellent vibration suppression effect. This is used as the evaluation standard.

Fig.7(a) shows the wave suppression level distribution of PGCM and n-PGCM in the range of excitation frequency from 11 to 23 kHz when the excitation is Excitation 1. The calculation effective area is still the same as shown in Figs.6(a)-(c). The yellow shaded areas in Fig. 7(a) represent the frequency bands where the wave suppression level achieved by the PGCM exceeds 6 dB. The gray shaded area (14.7-16.2 kHz, 16.6-22.8 kHz) is the frequency band where the vibration suppression of the PGCM is higher than that of the n-PGCM, which proves that the structure designed based on the total internal reflection theory has great advantages in broadband effect. The total bandwidth is 7.7 kHz.

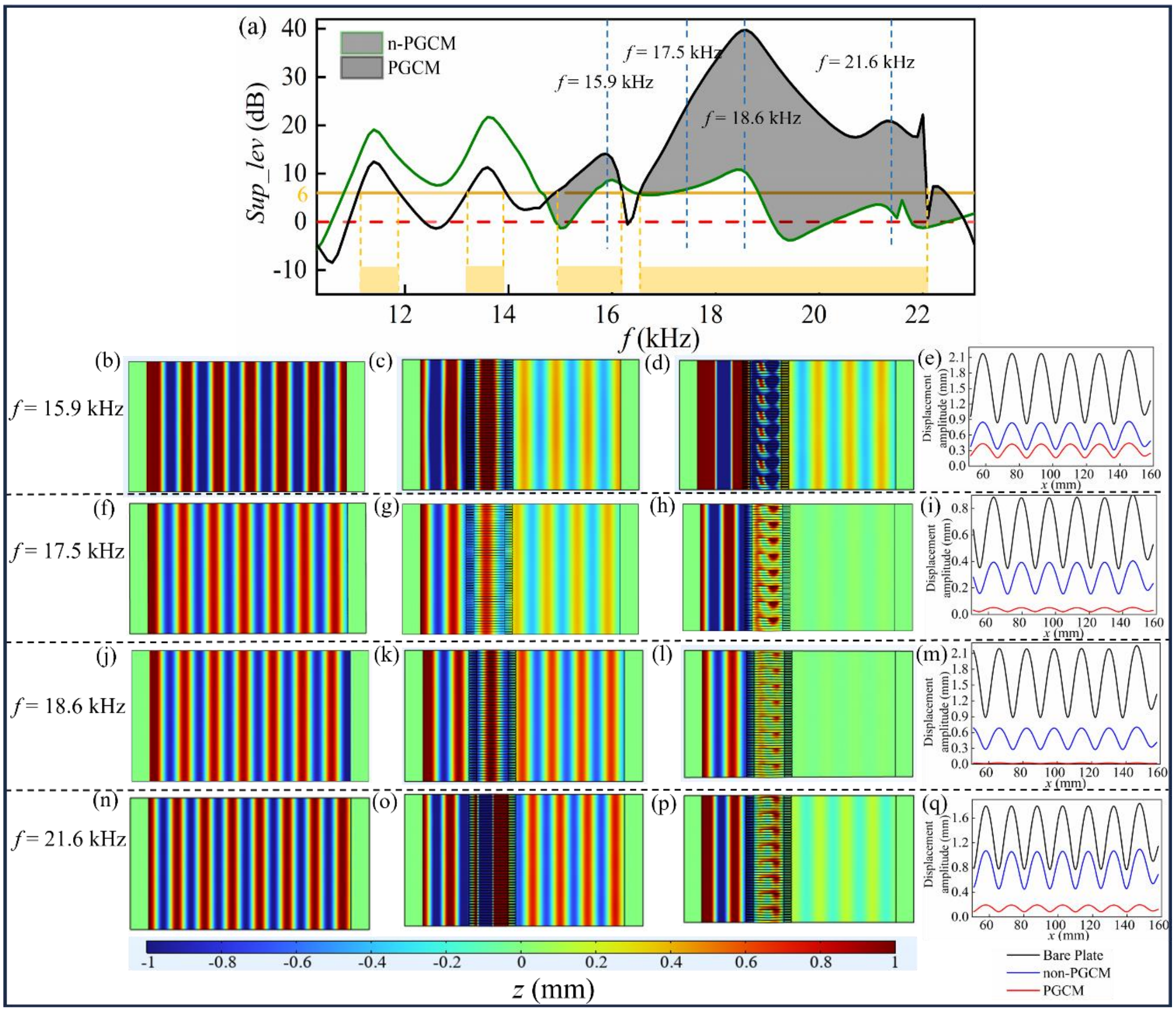

Fig.7. (a) Suppression level distribution of normal incident waves for PGCM and n-PGCM across different excitation frequencies under Excitation 1. (b)-(d), (f)-(h), (j)-(l), and (n)-(p): Out-of-plane displacement field distributions of the three corresponding structures, bare plate, n-PGCM, PGCM at 15.9 kHz, 17.5 kHz, 18.6 kHz, and 21.6 kHz, respectively. (e), (i), (m), and (q): Out-of-plane displacement amplitude distributions along the central axis of the three structures at 15.9 kHz, 17.5 kHz, 18.6 kHz, and 21.6 kHz, respectively.

In the gray-shaded area, four frequency points 15.9 kHz, 17.5 kHz, 18.6 kHz, and 21.6 kHz are selected. Figs.7(b)-(d), (f)-(h), (j)-(l), (n)-(p) are the surface displacement field distributions of the three structures at these four frequencies. Control the color bar to be consistent, and it can be seen that the color of the PGCM is the lightest, and n-PGCM is not necessarily lighter than the bare plate.

To more intuitively demonstrate the Lamb wave suppression effects of the n-PGCM and PGCM structures, we present the out-of-plane displacement amplitudes along the central axes of the scan areas for the three structures (indicated by the blue dashed lines L_1, L_2, and L_3 within the scan regions in Figs. 6(a)-(c)), as shown in Figs. 7(e), (i), (m), and (q). The results indicate that the out-of-plane displacement amplitude of the PGCM is lower than that of the n-PGCM, and even lower than that of the bare plate. Among the three structures, PGCM exhibits the most effective vibration suppression, particularly at f = 18.6 kHz. As indicated by the black solid line for PGCM in Fig. 7(a), the vibration suppression effect peaks at 39.72 dB, demonstrating that PGCM not only benefits from the curved beam structure (which is also presented in the n-PGCM) but also from its design based on the principles of total internal reflection.

Further, this paper analyzes the vibration suppression capability of PGCM under point source excitation, that is, omnidirectional vibration excitation. Fig. 8(a) shows the wave suppression level distribution of PGCM and n-PGCM in the range of 8~27kHz when the excitation is Excitation 2, as shown by the red dots in Figs. 6(a)-(c). The calculation effective area is still the same as shown in Fig.6. The yellow shaded area in Fig. 8(a) is the frequency bandwidth where the transmitted Lamb waves suppression achieved by PGCM is greater than 6dB. The gray-shaded areas (10.4-10.8 kHz, 11.2-12.5 kHz, 13.4-15.5 kHz, 16.3-27.5 kHz) are the frequency bands where the vibration suppression of the PGCM is higher than that of the n-PGCM. At f = 15.3 kHz, the black solid line representing the PGCM in Fig.8(a) reaches its peak, indicating that the vibration suppression effect is the best, which is 21.34 dB.

By selecting four frequency points, 11.5 kHz, 15 kHz, 19.2 kHz, and 24.3 kHz, within the gray-shaded regions, we adjusted the color bars to maintain consistency and plotted the out-of-plane displacement distributions for the three structures, as shown in Figs. 8(b)-(d), (f)-(h), (j)-(l), and (n)-(p). The results indicate that the PGCM structure exhibits the lightest color, demonstrating that the design based on the total internal reflection theory offers significant advantages in achieving a broadband effect for omnidirectional incident waves. Meanwhile, the amplitudes of the out-of-plane displacement along the axes (indicated by the blue dotted lines in Figs. 6(a)-(c)) of the three structures at the corresponding frequencies are presented in Figs. 8(e), (i), (m), and (q). The results show that the out-of-plane displacement amplitude of the PGCM structure is lower than that of the n-PGCM and the bare plate.

These findings demonstrate that the PGCM structure can meet more complex requirements, further validating the reliability of the design based on the total internal reflection theory.

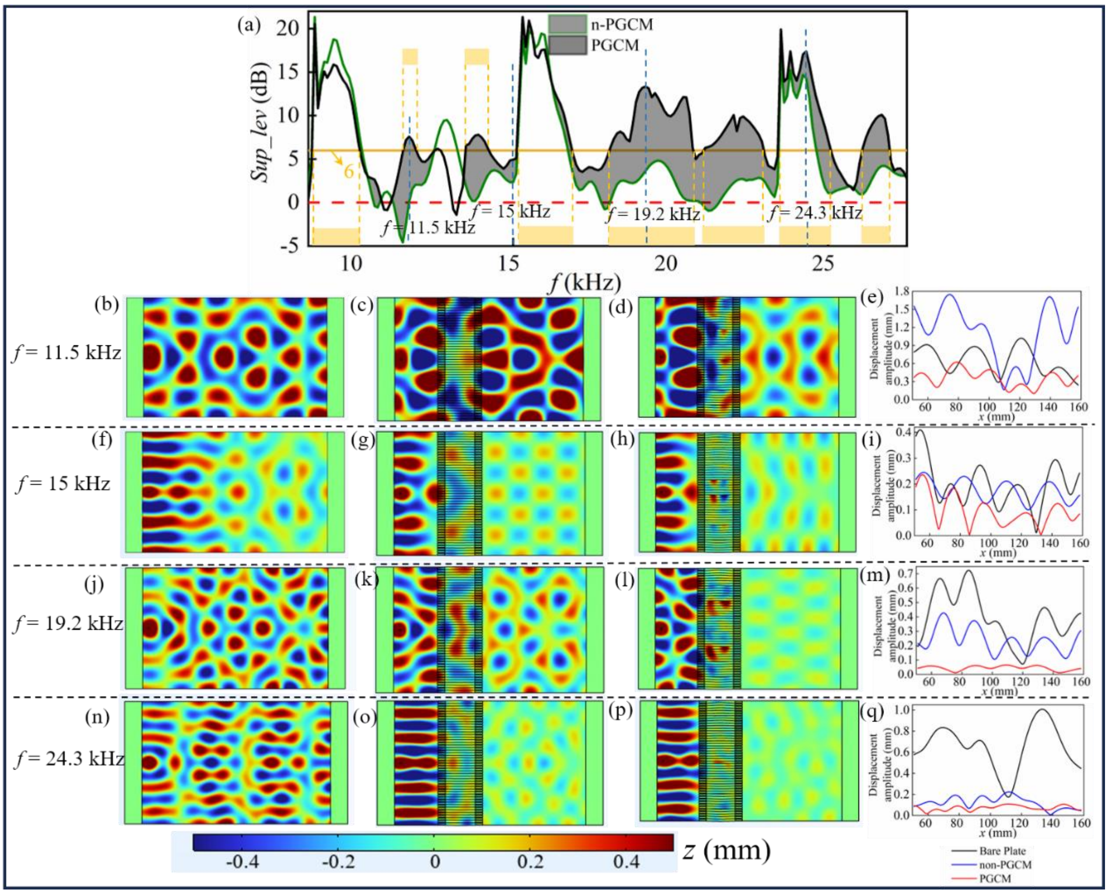

Fig.8. (a) Suppression level distribution of omnidirectional incident waves for PGCM and n-PGCM across different excitation frequencies under Excitation 2. (b)-(d), (f)-(h), (j)-(l), and (n)-(p): Out-of-plane displacement field distributions of the three corresponding structures, bare plate, n-PGCM, PGCM at 11.5 kHz, 15 kHz, 19.2 kHz, and 24.3 kHz, respectively. (e), (i), (m), and (q): Out-of-plane displacement amplitude distributions along the central axis of the three structures at 11.5 kHz, 15 kHz, 19.2 kHz, and 24.3 kHz, respectively.

The broadband performance of the proposed structure is attributed to its non-resonant nature, which stems from the TIR-based design. Unlike locally resonant structures that exhibit strong frequency selectivity near their resonance points, the PGCM operates independently of such narrowband resonance effects. As a result, it maintains effective wave manipulation over a wide frequency range.

Furthermore, the structure incorporates curved beam elements of varying sizes, which introduce diverse local resonance modes. Although the overall mechanism is non-resonant, these local resonances enhance reflection within specific frequency bands, further broadening the operational bandwidth. In addition, the PGCM is effective for Lamb wave incidence from various directions, which supports its omnidirectional and broadband reflective capabilities

3. Experimental verification

The cell structures of PGCM are produced by 3D printing to build an experimental platform to verify the results of the numerical simulation model. The experimental setup is shown in Fig. 9(a), and the sample layout is shown in Figs. 9 (b) and (c). Fig. 9 (d) is a partial enlargement of the periodic structure of PGCM. First, to reduce the impact of edge diffraction, 10 units are manufactured compared to the 8 units set in the simulation. The manufactured cell structures are bonded one by one to the upper surface of the thin plate (500 mm (L) × 300 mm (W) × 1 mm (T)) with special glue as shown in Fig. 9(c). A piezoelectric ceramic plate (20 mm (Diameter) × 1 mm (Thickness)) is bonded on the left side of the thin plate as the excitation, as shown in Figs. 9 (b) and (c) and connected to the power amplifier (AG1020). The laser scanning vibrometer (LSV), Polytec PSV-400, excites a sine signal with f = 15 kHz and a voltage of 20 V, which is then transmitted to the piezoelectric ceramic plate through the power amplifier.

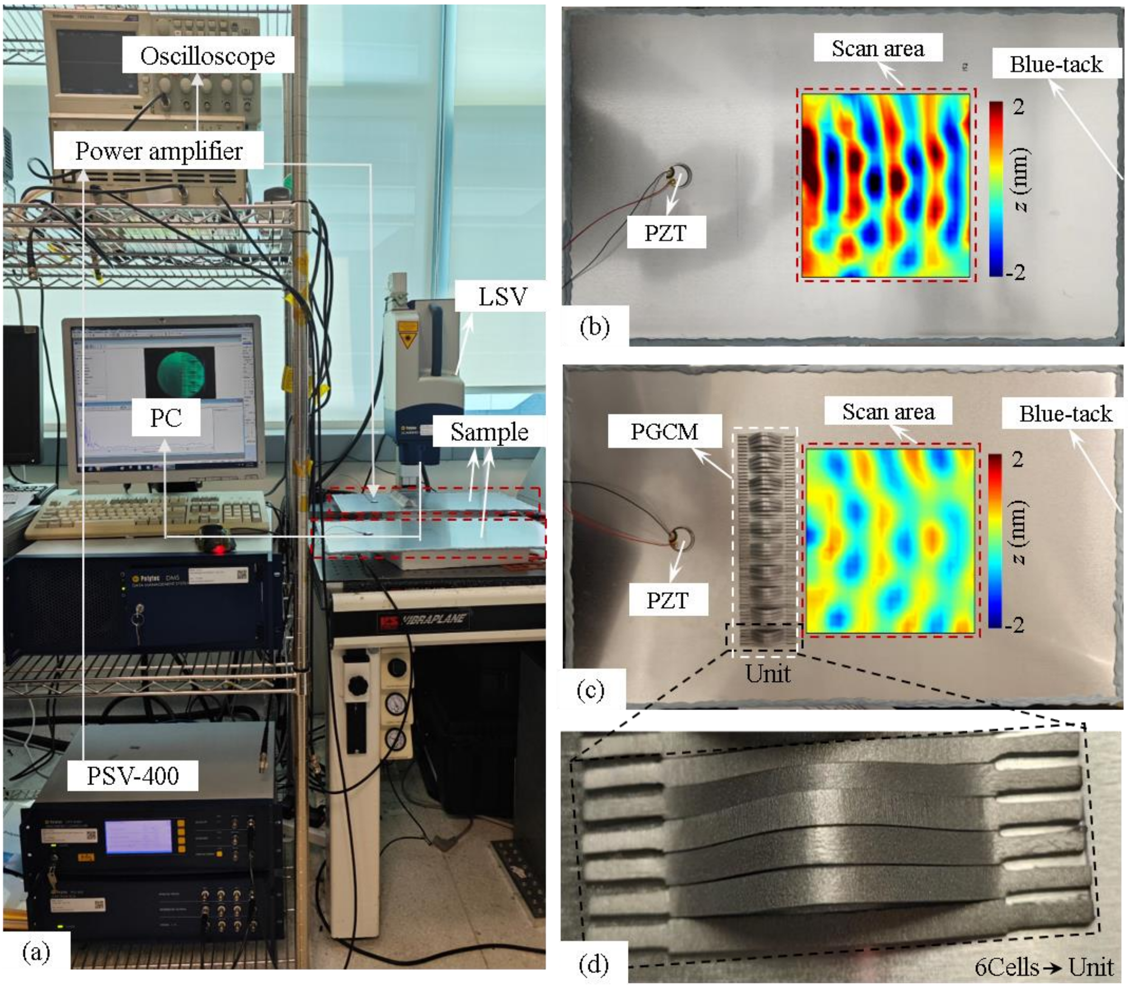

Fig.9. Experimental setup and the specimen. (a) Schematic diagram of the bare plate experimental sample and the out-of-plane displacement distribution in the scanning area. (b) Schematic diagram of the thin plate experimental sample with PGCM installed and the out-of-plane displacement distribution in the scanning area. (d) A partial enlargement of a periodic structure of PGCM.

The scan areas (126 mm (L) × 138 mm (W), as shown in Figs. 9 (b) and (c), corresponding to the pickup area size of 8 units in the simulation) are discretized. The out-of-plane displacements of all discrete points on the LSV pickup domain are analyzed by the analysis software PSV8.8 Acquisition on the PC to obtain the out-of-plane displacement distribution at the scan area, as shown in Figs. 9(b) and (c). A layer of Blu tack material is evenly pasted on the four edges of the thin plate to minimize the reflections. The color bars are controlled to be consistent. The results clearly show that the displacement distribution color of the plate with PGCM structure mounted is much lighter than that of the bare plate, which indicates that the PGCM has a good vibration suppression effect.

Subsequently, based on the bandwidth performance of the structure obtained from numerical simulations, a sine signal with a voltage of 20 V was excited using the LSV at frequencies of 8.93 kHz, 11.3 kHz, 15.5 kHz, 16.5 kHz, 20.28 kHz, 23.5 kHz, 23.66 kHz, and 24.3 kHz. The out-of-plane displacements of both the bare plate and the thin plate with the PGCM were measured at the corresponding positions within the scanning area, and the average amplitude of the out-of-plane displacement within this area was calculated. Considering that the experimental structure is finite-periodic, the free boundary conditions more closely approximate the actual physical boundaries under experimental conditions. Accordingly, the boundary conditions in the numerical simulation were modified, and the resulting data were compared with the experimental measurements, as shown in Fig. 10. The results show a high level of agreement between the simulations and the experimental data, further validating the effectiveness of the simulation approach. The minor deviations observed could be attributed to the following factors: (1) reflection waves at the plate edges even with absorption layer, (2) coupling effects between adjacent unit cells, and (3) manufacturing imperfections in the structure.

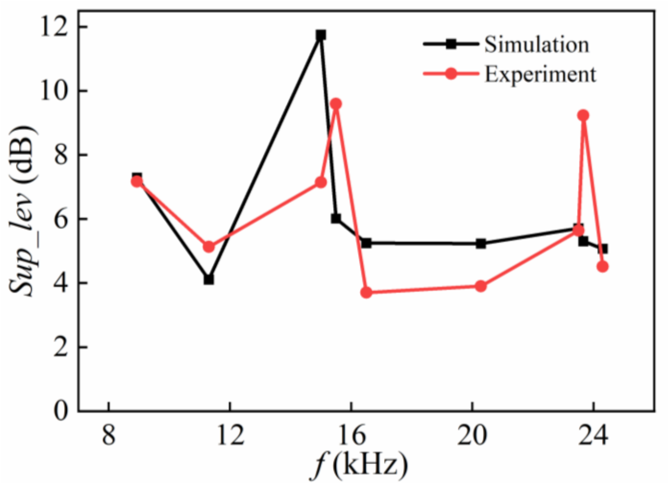

Fig.10. Comparison of wave suppression levels obtained by simulation and experiment.

Fig. 11 illustrates the out-of-plane displacement distributions of the bare plate and the PGCM-mounted thin plate at the corresponding scan area positions for frequencies of 11.3 kHz, 15.5 kHz, 23.5 kHz, and 24.3 kHz, respectively. To visually demonstrate the suppression performance of the PGCM, Figs. 11(i)-(l) present the amplitude profiles of out-of-plane displacement along the same axis (black dashed lines) for both the bare plate and the PGCM-mounted plate. The results of frequencies at 11.3 kHz, 15.5 kHz, 23.5 kHz clearly show that the displacement in the PGCM-mounted plate is significantly smaller than that in the bare plate. At 24.3 kHz, however, the displacement amplitudes along the central axis do not show a significant suppression effect for plate with PGCM, as seen in Fig. 11(l). This may be due to inconsistencies in the plate's support conditions, which result in the maximum displacement occurring off-axis in the bare plate. Nevertheless, the displacement fields in Figs. 11(d) and 11(h) still demonstrate a clear wave suppression effect by the PGCM.

This confirms the Lamb wave suppression effect of the PGCM. Moreover, the suppression observed across multiple frequencies indicates that the PGCM offers a broad suppression bandwidth, further validating the reliability of the simulation model.

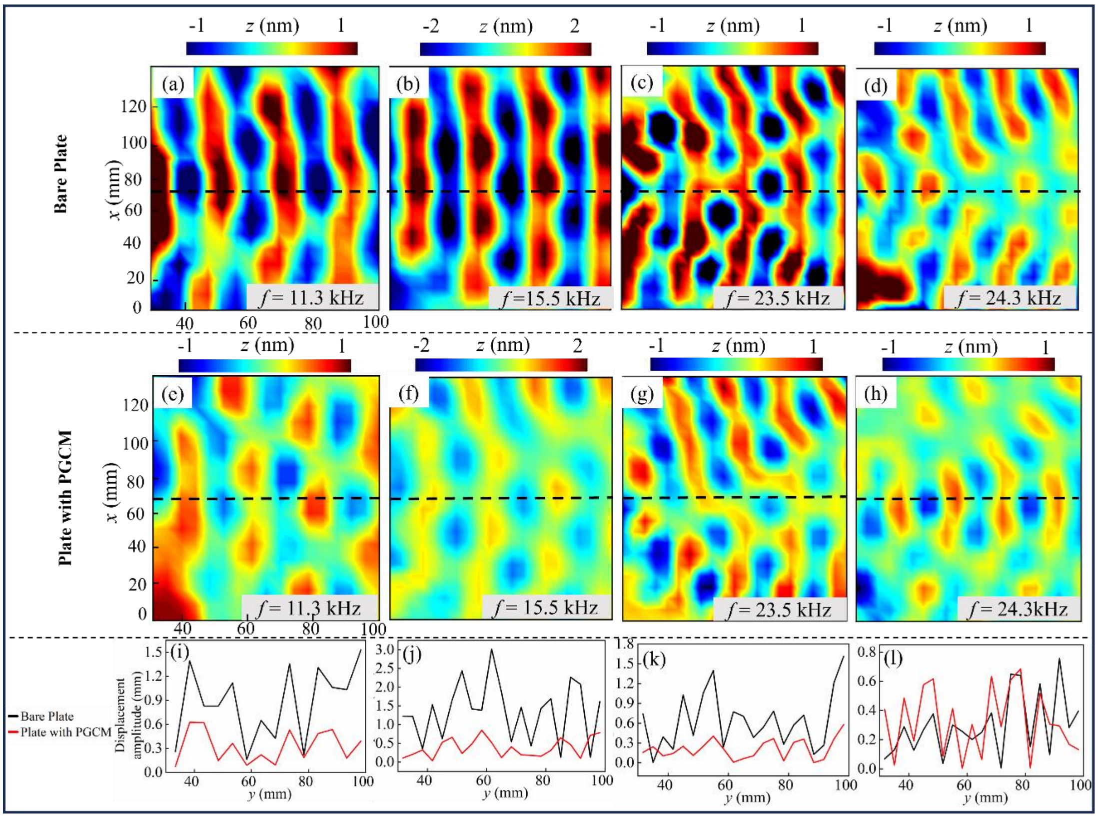

Fig.11. Out-of-plane displacement distributions for the bare plate and the PGCM-mounted thin plate at the same scanning area. (a-d) Displacement distributions of the bare plate at frequencies of 11.3 kHz, 15.5 kHz, 23.5 kHz, and 24.3 kHz, respectively. (e-h) Displacement distributions of the PGCM-mounted thin plate at the same frequencies and positions. (i–l) Out-of-plane displacement

amplitude profiles along the central axis for both the bare plate and the PGCM-mounted plate at the corresponding four frequencies.

4. Conclusions

In this paper, we designed a PGCM for vibration suppression of omnidirectional incident waves based on the generalized Snell's law and the theory of total internal reflection. By adjusting the height of the curved beam, the transmitted phase of Lamb waves is modulated within a full 2π range, enabling effective phase control. The structure exhibits high flexibility, making it well-suited for complex vibration control applications.

A key advantage of the design lies in the use of discrete adjacent cell structures, which preserve the integrity of the host structure while minimizing coupling effects. Numerical analysis demonstrates the broadband effectiveness of the proposed PGCM, achieving maximum vibration suppression of 39.72 dB for normal incident waves and 21.34 dB for omnidirectional waves. Furthermore, comparisons with the n-PGCM confirm superior suppression performance.

Experimental tests verified both the effectiveness and reliability of the PGCM, with additional tests confirming its broadband suppression capabilities at other frequencies. The proposed design is not only simple to fabricate and cost-effective but also holds significant potential for practical applications in vibration control.

Author contributions

Shuzhen Huang: Conceptualization, Methodology, Investigation, Writing-original draft, Validation. Lei Zhang: Conceptualization, Methodology, Funding acquisition, Writing-review & editing. Guilin Wen: Methodology, Funding acquisition. Tham Zi Wen: Validation. Shan Yin: Methodology. Jie Liu: Investigation, Funding acquisition.

Acknowledgments

This work is funded by the China Scholarship Council, Grant No.202306130082 (Shuzhen Huang), the Key Program of the National Natural Science Foundation of China, Grant No.

12332002 (Guilin Wen), and Hebei Natural Science Foundation of China, Grant No. A2024203026 (Jie Liu). This work is supported by MTC Individual Research Grant (IRG), Grant No. M22K2c0090, Singapore (Lei Zhang).

Declaration of competing interest

The authors declare that they have no known competing financial interests or personal relationships that could have appeared to influence the work reported in this paper.

Data availability

Data will be made available on reasonable request.

References

[1] Z.R. Wani, M. Tantray, E.N. Farsangi, N. Nikitas, M. Noori, B. Samali, T.Y. Yang. A critical review on control strategies for structural vibration control. Annu Rev Control 54 (2022) 103-124.

[2] D. Karnopp. Active and semi-active vibration isolation. (1995) 177-185.

[3] R.A. Ibrahim. Recent advances in nonlinear passive vibration isolators. J sound vib 314.3-5 (2008) 371-452.

[4] R. Alkhatib, M.F. Golnaraghi. Active structural vibration control: a review. Shock Vibr Dig 35.5 (2003) 367.

[5] J.Q. Sun, M.R. Jolly, M.A. Norris. Passive, adaptive and active tuned vibration absorbers—a survey. (1995) 234-242.

[6] E.M. Jr Kerwin. Damping of flexural waves by a constrained viscoelastic layer. J Acoust soc Am 31.7 (1959) 952-962.

[7] Y. Song, J. Wen, D. Yu, X. Wen. Suppression of vibration and noise radiation in a flexible floating raft system using periodic structures. J Vib Control 21.2 (2015) 217-228.

[8] H. Peng, P.F. Pai. Acoustic metamaterial plates for elastic wave absorption and structural vibration suppression. Int J Mech Sci 89 (2014) 350-361.

[9] J.M. Kweun, H.J. Lee, J.H. Oh, H.M. Seung, Y.Y. Kim. Transmodal Fabry-Pérot resonance: theory and realization with elastic metamaterials. Phys rev lett 118.20 (2017) 205901.

[10] H.K. Zhang, Y. Chen, X.N. Liu, G.K. Hu. An asymmetric elastic metamaterial model for elastic wave cloaking. J Mech Phys Solids 135 (2020) 103796.

[11] M. Badreddine Assouar, M. Senesi, M. Oudich, M. Ruzzene, Hou Z. Broadband plate-type acoustic metamaterial for low-frequency sound attenuation. Appl Phys Lett 101.17 (2012).

[12] J. Ma. Phonon Engineering of Micro-and Nanophononic Crystals and Acoustic Metamaterials: A Review. Small Sci 3.1 (2023) 2200052.

[13] T. Vasileiadis, J. Varghese, V. Babacic, J. Gomis-Bresco, D.N. Urrios, B. Graczykowski. Progress and perspectives on phononic crystals. J Appl Phys 129 (2021) 160901.

[14] Z. Boqiang, Z. Qiangqiang, H. Qingwen, F. Tianpei, X. Gao, J. Xin. Bandgap Mechanism of Phonon Crystals Coupled to Acoustic Black Holes. Acoust Phys 70.3 (2024) 453-464.

[15] Y. Li, S. Yan, Y. Peng. Broadband vibration attenuation characteristic of 2D phononic crystals with cross-like pores. Thin Wall Struct 183 (2023) 110418.

[16] N. Yu, P. Genevet, M.A. Kats, F. Aieta, J.P. Tetienne, F. Capasso. Light propagation with phase discontinuities: generalized laws of reflection and refraction. Sci 334.6054 (2011) 333-337.

[17] H.T. Chen, A.J. Taylor, N. Yu. A review of metasurfaces: physics and applications. Rep prog Phys 79.7 (2016) 076401.

[18] S.S. Bukhari, J. Vardaxoglou, W. Whittow. A metasurfaces review: Definitions and applications. Appl Sci 9.13 (2019) 2727.

[19] B. Assouar, B. Liang, Y. Wu, Y. Li, J.C. Cheng, Y. Jing. Acoustic metasurfaces. Nat Rev Mat 3.12 (2018) 460-472.

[20] J. Guo, R. Qu, Y. Fang, W. Yi, X. Zhang. A phase-gradient acoustic metasurface for broadband duct noise attenuation in the presence of flow. Int J Mech Sci 237 (2023): 107822.

[21] H. Tang, Z. Hao, J. Zang. Nonplanar acoustic metasurface for focusing. J Appl Phys 125.15 (2019).

[22] Y. Li, B.M. Assouar. Acoustic metasurface-based perfect absorber with deep subwavelength thickness. Appl Phys Lett 108.6 (2016).

[23] J. Guo, R. Qu, Y. Fang, W. Yi, X. Zhang. A phase-gradient acoustic metasurface for broadband duct noise attenuation in the presence of flow. Int J Mech Sci 237 (2023) 107822.

[24] Y. Li, C. Shen, Y. Xie, J. Li, W. Wang, S.A. Cummer, Y. Jin. Tunable asymmetric transmission via lossy acoustic metasurfaces. Phys rev lett 119.3 (2017) 035501.

[25] S. Huang, G. Wen, S. Yin, Z. Lv, J. Liu, Z. Pan, L. Jia. Tunable acoustic metasurface for broadband asymmetric focusing based on Helmholtz resonator. J Sound Vib 591 (2024) 118628.

[26] F. Liu, P. Shi, Y. Shen, Y. Xu, Z. Y ang. Advances in suppression of structural vibration and sound

radiation by flexural wave manipulation. Thin Wall Struct 200 (2024) 111936.
[27] L. Cao, Z. Yang, Y. Xu, S.W. Fan, Y. Zhu, Z. Chen, Y. Li, Assouar B. Flexural wave absorption by lossy gradient elastic metasurface. J Mech Phys Solids 143 (2020) 104052.
[28] X. Huang, J. Su, L. Ren, H. Hua. Development of curved beam periodic structure in broadband resonance suppression for cylindrical shell structure. J Vib Control 23.8 (2017) 1267-1284.
[29] L. Cao, Z. Yang, Y. Xu, S.W. Fan, Y. Zhu, Z. Chen. Disordered elastic metasurfaces. Phys Rev Appl 13.1 (2020) 014054.
[30] H. Zhu, T.F. Walsh, F. Semperlotti. Total-internal-reflection elastic metasurfaces: Design and application to structural vibration isolation. Appl Phys Lett 113.22 (2018).
[31] H. Zhu, T.F. Walsh, F. Semperlotti. Experimental study of vibration isolation in thin-walled structural assemblies with embedded total-internal-reflection metasurfaces. J Sound Vib 456 (2019) 162-172.
[32] H. Zhu, T.F. Wal sh, B.H. Jared, F. Semperlotti. On the broadband vibration isolation performance of nonlocal total-internal-reflection metasurfaces. J Sound Vib 522 (2022) 116670.
[33] Y. Shen, Y. Xu, F. Liu, Z. Yang. Metasurface-guided flexural waves and their manipulations. Int J Mech Sci 257 (2023) 108538.
[34] Y. Liu, Z. Liang, F. Liu, O. Diba, A. Lamb, J. Li. Source illusion devices for flexural lamb waves using elastic metasurfaces. Phys rev lett 119.3 (2017) 034301.
[35] H. Yang, et al. Lamb wave propagation control based on modified GSL. Front Phys 10(2022): 909318.
[36] W. Xu, M. Zhang, J. Ning, W. Wang, T. Yang. Anomalous refraction control of mode-converted elastic wave using compact notch-structured metasurface. Mater Res Express 6.6 (2019) 065802.
[37] W. Xu, M. Zhang, Z. Lin, C. Liu, W. Qi, W. Wang. Anomalous refraction manipulation of Lamb waves using single-groove metasurfaces. Phy Scripta 94.10 (2019) 105807.
[38] S.M. Yuan, A.L. Chen, Y.S. Wang. Switchable multifunctional fish-bone elastic metasurface for transmitted plate wave modulation. J Sound Vib 470 (2020) 115168.
[39] Y. Jiang, Y. Liu, N. Hu, J. Song, D. Lau. Continuous-phase-transformation elastic metasurface for flexural wave using notched structure. Int J Mech Sci 257 (2023) 108563.
[40] X. Cao, et al. Excitation and manipulation of guided shear-horizontal plane wave using elastic metasurfaces. Smart Mater Struct 30.5 (2021): 055013.

[41] X. Zhang, et al. A subwavelength sinusoidally-shaped phononic beam structures-based metasurface for flexural wave steering. Appl Acoust 194 (2022): 108790.

[42] M. Li, Y. Hu, J. Cheng, J. Chen, Z. Li, B. Li. Elastic metasurfaces with tailored initial phase for broadband subwavelength focusing. Int J Mech Sci 268 (2024) 109048.

[43] L. Cao, Y. Xu, B. Assouar, Z. Yang. Asymmetric flexural wave transmission based on dual-layer elastic gradient metasurfaces. Appl Phys Lett 113.18 (2018).

[44] M. Farhat, W. Ying. Flexural zero-space waveguide arrays for waves in thin-elastic plates. Thin Wall Struct (2024) 112682.

[45] H. Yang, K. Feng, R. Li. Lamb wave transmission control based on elastic wave metasurface [in Chinese]. J Appl Acoust 42.1(2023).

[46] Z.L. Xu, D.F. Wang, Y.F. Shi, Z.H. Qian, B. Assouar, K.C. Chuang. Arbitrary wavefront modulation utilizing an aperiodic elastic metasurface. Int J Mech Sci 255 (2023) 108460.

[47] Y. Jin, B. Bonello, R.P. Moiseyenko, Y Pennec, O. Boyko. Djafari-Rouhani B. Pillar-type acoustic metasurface. Phys Rev B 96.10 (2017) 10431.

[48] Y. Jin, W. Wang, A. Khelif, B. Djafari-Rouhani. Elastic metasurfaces for deep and robust subwavelength focusing and imaging. Phys Rev Appl 15.2 (2021) 024005.

[49] W. Wang, J. Iglesias, Y. Jin, B. Djafari-Rouhani, A. Khelif. Experimental realization of a pillared metasurface for flexural wave focusing. Apl Mater 9.5 (2021).

[50] L. Cao, Z. Yang, Y. Xu, B. Assouar. Deflecting flexural wave with high transmission by using pillared elastic metasurface. Smart Mater Struct 27.7 (2018) 075051.

[51] L. Cao, Z. Yang, Y. Xu, Z. Chen, Y. Zhu, S.W. Fan, K. Donda, B. Vincent, B. Assouar. Pillared elastic metasurface with constructive interference for flexural wave manipulation. Mech Syst Signal Pr 146 (2021) 107035.

[52] H. Jeffreys, Jeffreys B. Methods of mathematical physics. Cambridge university press 1999.

[53] W.P. Rogers. Elastic property measurement using Rayleigh-Lamb waves. Res Nondestruct Eval 6.4 (1995) 185-208.

[54] L.E. Pitts, T.J. Plona, W.G. Mayer. Theoretical similarities of Rayleigh and Lamb modes of vibration. J Acoust Soc Am 60.2 (1976) 374-377.

[55] M.D. Gilchrist. Attenuation of ultrasonic Rayleigh–Lamb waves by small horizontal defects in thin aluminium plates. Int J Mech Sci 41.4-5 (1999) 581-594.